Shock Waves (2010) 20:339–345
DOI 10.1007/s00193-010-0265-z

TECHNICAL NOTE

Modulations of a weak shock wave through a turbulent slit jet

Jae-Hyung Kim · Akihiro Sasoh · Atsushi Matsuda

Received: 1 September 2009 / Revised: 12 June 2010 / Accepted: 28 June 2010 / Published online: 17 July 2010

Abstract The pressure modulation of a weak shock wave induced by a Nd:YAG laser pulse when passing across a turbulent slit jet was experimentally investigated. With the slit jet the peak overpressure became smaller by an average of 12%, with a standard deviation of 27%. Clear relationships were obtained between the overpressure history and the experimentally observed shock front deformation, which was visualized as differential schlieren images. The peak overpressure was increased when the originally spherical blast wave front was locally flattened, whereas it was decreased when a hump in the shock wave front was formed.

Keywords Shock wave · Turbulence · Sonic boom · Compressible flow

1 Introduction

The behavior of a weak shock wave is a fundamental problem both in compressible fluid dynamics and in nonlinear acoustics. For instance, the so-called 'von Neumann paradox' [1,2] is a problem of oblique shock wave reflection occurring when the reflected wave is so weak at the intersection with the incident shock wave that its behavior is not simply determined from the three-shock theory. The sonic boom is another example in which weak shock wave behavior is complex when propagating over a long distance [3–5]. In sonic boom propagation, its peak overpressure and waveform characteristics are varied depending on the propagation medium and/or topography. In particular, when a shock wave propagates through turbulence, the post-shock pressure field is significantly modulated. However, current understanding of the associated mechanisms is quite limited.

The interactions between a shock wave and a vortex have been extensively studied. Ribner [6] obtained an analytical expression of acoustic wave emission caused by shock-vortex interaction from a linear theory. Ellzey et al. [7] classified shock-vortex interaction into weak and strong cases. The weak interaction involves small shock wave deformation and acoustic wave emission which could be predicted by the linear theory. The strong interaction involves large shock wave deformation, and leads to the formation of complex shock patterns. Chatterjee [8] reported that the type of shock pattern formed in compressible vortex-shock wave interaction depends strongly on the incident shock Mach number. Three-dimensional shock deformation resulting from the interaction between a spherical shock wave and a vortex ring was studied in Refs. [9,10]. Although the mechanisms of shock wave distortion due to vortices were well understood, the impact of the shock-vortex interaction on post-shock pressure modulation was not of primary interest.

The post-shock pressure modulations resulting from interaction with jets were studied by Ribner et al. [11] who used a conical shock tube. In this study, the jet blew either in the same or in the opposite direction of the shock wave propagation. Figure 1a shows the conventional overpressure profile without turbulence. An overpressure spike occurs in the leading part of a typical N-shaped pressure profile of the blast front (Fig. 1b) when the jet opposes the shock front, while the interaction of the shock wave with a jet in the same

Communicated by H. Kleine.

This paper was based on work that was presented at the 27th International Symposium on Shock Waves, St. Petersburg, Russia, 19–24 July 2009.

J.-H. Kim (✉) · A. Sasoh · A. Matsuda
Department of Aerospace Engineering, Nagoya University, Nagoya, Aichi 464-8603, Japan
e-mail: jhkim@fuji.nuae.nagoya-u.ac.jp

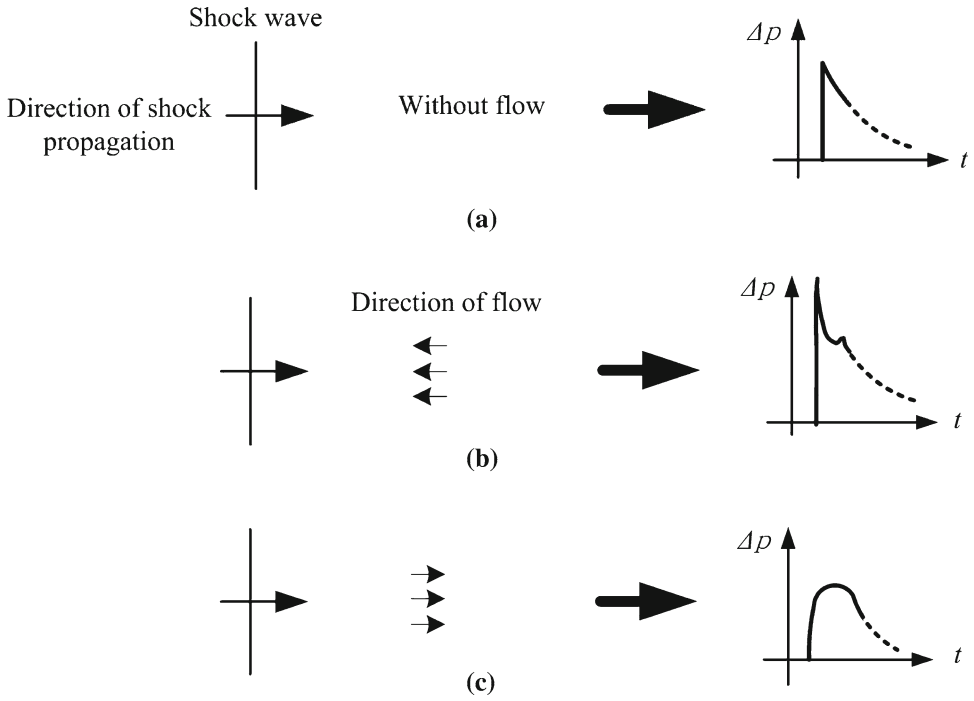

Fig. 1 Overpressure rise patterns after shock wave-flow interaction; **a** without disturbance, **b** spiked (flow in the opposite direction to shock propagation), **c** rounded (flow in the same direction as of shock propagation)

direction leads to a rounded variation (Fig. 1c). Pierce [12] argued that these pressure modulations could be modeled based on geometrical acoustics.

Many studies on sonic booms generated by supersonic aircraft dealt with the interaction of a shock wave and a turbulent flow. The primary interest of this topic is the modulation of the peak value and the rise time of the overpressure variation. Pierce [13] reviewed the extent of the variability in overpressure waveforms recorded during actual flight tests. The random nature of the waveform variability was classified into several types: a high peak overpressure corresponded to a spiked waveform, while a low one corresponded to a rounded waveform.

Lipkens and Blackstock [14] conducted laboratory model experiments of a weak shock wave modulation through a turbulent flow. A shock wave was generated using an electric spark and a turbulent jet flow was ejected from a slit. The turbulence caused enormous variability in the waveform of the post-shock overpressure. On average, the slit jet led to an increase in the rise time and a decrease in the peak overpressure. However, the standard deviation became much larger than the average decrement, which implied that in some cases the peak overpressure was enhanced although mostly it was weakened. Such 'statistical' behavior cannot be reproduced by deterministic computational fluid dynamics simulation [15]. The associated mechanisms of the pressure modulation warrant further investigation, specifically to determine under what conditions the shock strength is increased or decreased, and how the shock shape is deformed in the interaction process.

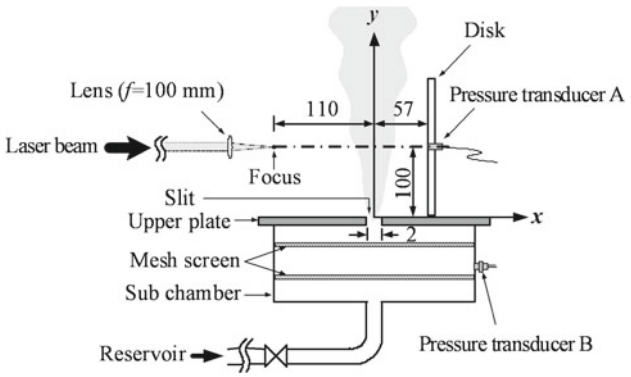

Fig. 2 Schematic illustration of experimental set-up (not true to scale) (units in mm)

The purpose of this study is to advance the understanding of the interaction mechanisms between a weak shock wave and a turbulent flow, highlighting the experimental relations between shock wave front deformation and post-shock overpressure modulation.

2 Experimental method

A schematic diagram of the experimental setup is given in Fig. 2. A blast wave, a shock wave immediately followed by an expansion zone, is generated by focusing a Nd:YAG laser pulse (wavelength of 1,064 nm, FWHM of 9 ns, output energy of 0.45 J) using a convex lens with a focal length of 100 mm. The overpressure is measured on a 200 mm diameter, 5 mm

thick aluminum disk at 167 mm from the focus with a central, flush-mounted piezoelectric pressure transducer (PCB Piezoelectronics, Inc. Model-HM102A18, rise time of 1 μs, natural frequency of 500 kHz). The axis of the disk is aligned to the direction of shock wave propagation. A sheet of shear flow from a slit on the upper plate of a stainless steel sub-chamber of an inner volume of 0.014 m^3, which hereafter will be referred to as the 'slit jet,' is supplied normal to the shock wave propagation direction. The sub-chamber overpressure from the atmospheric value (Δp_s) is kept at 20 kPa. The distance between the focus point of the laser, i.e., the center of the blast wave, and the slit jet is set to 110 mm. It is noted that all tests were conducted under identical and controlled atmospheric conditions.

The signal of pressure transducer A (resolution: 3.4 Pa; sampling rate: 10 M samples/s) is the overpressure generated by the reflection of the laser-induced blast wave from the disk surface. Expansion waves originating at the disk periphery arrive at the pressure transducer about 580 μs after the initiation of the overpressure rise due to the blast wave. As will be seen later, the overpressure of present interest lasts about 60 μs. During this period, the overpressure signal is not affected by the finite size of the disk. Although the uncertainty of the pressure transducer which the manufacturer claims equals ±0.8%, the measured overpressure signal contained larger oscillatory components of the natural frequency. As much as possible, this component was eliminated in designing the transducer mount so as not to violate the validity and generality of the following results.

The x- and y-axes are defined as shown in Fig. 2. The z-axis, not shown in the figure, is perpendicular to the plane of the paper. The x–z plane includes the surface of the upper plate ($-150\,\text{mm} \le x \le 150\,\text{mm}$, $-150\,\text{mm} \le z \le 150\,\text{mm}$). The slit has a rectangular shape with a width of 2 mm ($-1\,\text{mm} \le x \le 1\,\text{mm}$) and a length of 200 mm($-100\,\text{mm} \le z \le 100\,\text{mm}$). The slit jet flows along the y–z plane, primarily in the y direction. The disk axis and the focus are on a line of $y = 100$ mm and $z = 0$ mm, parallel to the x-axis.

Distributions of the y-component of the flow velocity and its fluctuation on the $z = 0$ plane are measured using a constant temperature anemometer (CTA) type hot-wire. The hot-wire has a diameter of 5 μm. The output signals are recorded with a digital oscilloscope at a sampling frequency of 20 kHz. Hot-wire calibrations were conducted using a Pitot probe which was placed side-by-side in a low-turbulence wind tunnel [16] where the turbulence intensity is estimated to be lower than 0.18%.

A schlieren optical system is used to visualize shock wave motions. It consists of two 300- mm diameter concave mirrors (focal length 3 m) and a xenon flash lamp with a light intensity of about 10 kW/sr and a nominal duration time of 200 μs. A knife edge placed at the focal point of the schlieren optics vertically cuts off about half of the object beam. One hundred images are sequentially taken using a high speed framing camera (Shimadzu Co., HyperVision HPV-1) with a resolution of 312 × 260 pixels, a framing rate of 125,000 frames per second and a frame exposure time of 1 μs.

In the present experiments, the shock Mach number upon the disk, evaluated from the overpressure on the pressure transducer A, is approximately 1.007, corresponding to a density jump of 2.5% of the atmospheric density. With our optical setup, such a weak shock wave front yields a schlieren image of poor contrast. In order to improve the quality of the flow visualization, a differential image is numerically obtained by subtracting a gray-scale schlieren image of a past moment (reference image) from that at the moment of the interest (object image). Since the intensity of the xenon flash lamp varies during its duration, the time difference between two images was chosen within 80 μs so that the change in the contrast was sufficiently small. This image processing step allows one to eliminate the steady-state background noise in the area ahead of the shock wave while it also displays the shock wave and the associated flow with much enhanced contrast. As will be seen later, the shock wave shape is much more clearly obtained.

3 Results and discussion

Figure 3 presents the velocity distribution of the turbulent flow field in the x–y plane ($z = 0$), measured by a hot-wire anemometer. This measurement was conducted without the disk. At $y = 50$ mm, the slit jet has a slight saddle-back profile because of vena contracta effects. The full width at half maximum (FWHM) of $\bar{u}$ is estimated to be 26 mm at $y = 100$ mm, then increases by 37.5 mm at $y = 200$ mm. This velocity distribution is slightly disturbed by the disk at $x = 57$ mm. Due to the entrainment of mass flow, the centerline ($x = 0$ mm) velocity is gradually decreased along the y-direction; 31.5 m/s at $y = 100$ mm and 21.0 m/s at $y = 200$ mm. The flow field is almost symmetric; the extent of asymmetry in the mean velocity is smaller than 7.8%. The turbulence intensity is referred as the ratio of the root mean square of velocity fluctuation (u_{rms}) to the mean velocity ($\bar{u}_0$) at $x = 0$ mm, $y = 100$ mm and $z = 0$ mm. The turbulence intensity in Fig. 3b has a saddle-back distribution near the slit. At $y = 100$ mm, the peak value of the turbulence intensity equals 17.5% at $x = 10$ mm. Then, the peak value is decreased and the distribution is converted into an almost top-hat shape downstream. The peak value at $x = 0$ mm and $y = 200$ mm equals 11.8%. The Reynolds number of the slit jet is evaluated at 4.7×10^4 based on $\bar{u}_0 (= 31.5\,\text{m/s})$ and the FWHM of the slit jet velocity profile is 27 mm at the reference point $x = 0$ mm, $y = 100$ mm and $z = 0$ mm.

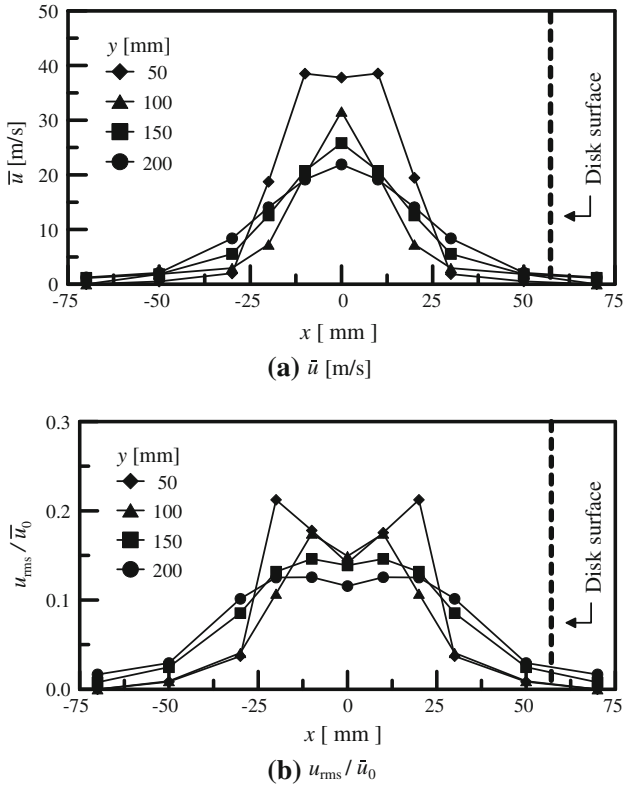

Fig. 3 Distributions of $\bar{u}$ and $u_{\mathrm{rms}}/\bar{u}_0$ measured without the disk on x–y plane; $\Delta p_s = 20$ kPa. Disk position is indicated for reference purposes

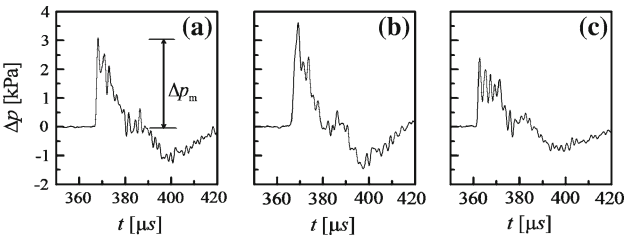

Fig. 4 Examples of overpressure histories measured with pressure transducer A; **a** without slit jet, **b** with slit jet (strong case) and **c** with slit jet (weak case)

Figure 4 presents a typical overpressure (Δp) history without slit jet (a) and with slit jet (b and c). Here, the time origin, $t = 0$, is at the laser pulse initiation. The differential schlieren images are shown in Fig. 5, where a–c correspond to the respective symbols in Fig. 4. Each image is subdivided into four regions A to D, see Fig. 5d. Region A is a differential schlieren image between $t = 96$ and 40 μs. A shock wave at $t = 96$ μs is seen as the black belt at the far right part of this region. The thickness of the belt corresponds to the distance the shock travels during exposure time of the high-speed imaging. Also a shock wave at $t = 40$ μs is visualized as a white ring, which is a result of the differential image processing. In the same way, region B corresponds to an image at 176 μs obtained from differentiation between 176

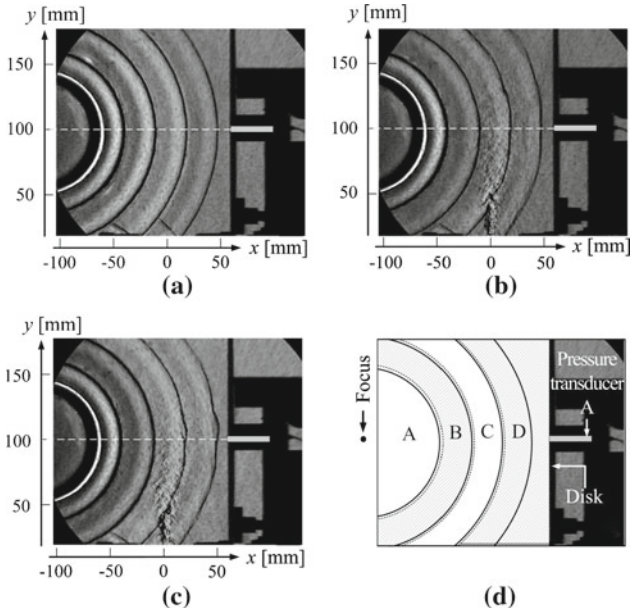

Fig. 5 Sequential visualization images corresponding to Fig. 4; **a** without slit jet, **b** with slit jet (strong case), **c** with slit jet (weak case) and **d** region of instants (*dashed line* boundary, *solid line* shock wave) *A*; differential schlieren image between $t = 96$ μs and $t = 40$ μs, *B*; differential schlieren image between $t = 176$ μs and $t = 96$ μs, *C*; differential schlieren image between $t = 256$ μs and $t = 176$ μs, *D*; differential schlieren image between $t = 336$ μs and $t = 256$ μs.

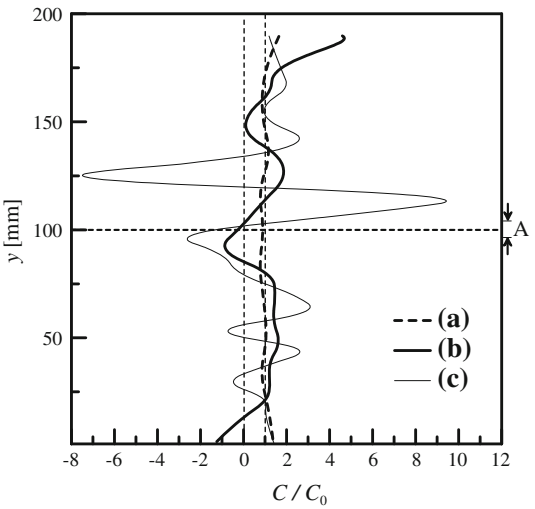

Fig. 6 Shock wave curvature distributions along y-axis at $t = 336$ μs; **a** without slit jet (Fig. 4a), **b** strong case (Fig. 4b) and **c** weak case (Fig. 4c). The regime marked by the *arrows* on the right side of the graph indicates the location of the pressure transducer A on the disk surface

and 96 μs, C at 256 μs from 256 to 176 μs, and D at 336 μs from 336 to 256 μs, respectively. In this way, in each image four shock waves at $t = 96$, 176, 256, 336 μs are visualized as dark shadows; an expansion region behind each shock wave is recognized as a bright zone. Figure 6 shows the distributions of shock front curvature evaluated from Fig. 5a–c

at $t = 336\,\mu s$. The distributions of the local curvature C are normalized to the curvature of a perfectly spherical blast wave (C_0). After digitizing the x–y location of a shock wave front, it is fitted to a b-spline function using fourth order base functions. The inherent measurement uncertainty is estimated approximately 0.5 mm, based on the size of the field of view and the resolution of the camera.

The curvature measured without the slit jet, case (a), is almost constant and close to the spherical case (see Fig. 6). As seen in Fig. 4a, when the shock wave reflects from the pressure transducer, the overpressure suddenly increases to a maximum value $\Delta p_{m,0} = 3.1$ kPa, which corresponds to a local shock Mach number of 1.007. Then, due to expansion, the overpressure decreases. The secondary shock wave [17] caused by the driver gas implosion appears as a small peak at $t = 385\,\mu s$. After the secondary shock wave, the overpressure further decreases to a negative value. At around $t = 400\,\mu s$, the overpressure starts to recover toward the atmospheric value. This overpressure variation shows the typical pressure history of a laser-induced blast wave [17]. The post-shock overpressure lasts for about 60 μs. The disturbance originating from the sub-chamber surface (which may contaminate the overpressure history) arrives thereafter, at about 194 μs after the impingement of the shock wave onto the pressure transducer A.

In both cases (b) and (c), before the shock wave passes the slit jet ($t = 176\,\mu s$), the distortion of the spherical shock front shape is negligible. However, the shock wave becomes distorted when passing through the jet ($t = 256$ and $336\,\mu s$). In the case of (b), as seen in Figs. 5b and 6, the normalized curvature of the shock front near the pressure transducer is decreased, having a flat shape and almost resembling a straight normal shock. As seen in Fig. 4b, the peak value of the overpressure, Δp_m, is increased to 3.5 kPa. Hereafter, such a case will be referred to as the 'strong case.' In the case of (c) in Figs. 4 and 5, the shock front has a hump slightly above the pressure transducer. As seen in Fig. 6, the curvature strongly oscillates and has a large positive peak. The local shock strength is weakened, having a smaller peak value of 2.3 kPa ('weak case,' hereafter).

Figure 7 presents the probability histogram of the peak overpressure measured with the slit jet obtained from fifty measurements. With the slit jet, the number of events has a maximum at around $\Delta p_m / \Delta p_{m,0} = 0.7 \pm 0.05$, spread from 40 to 160% of that without the slit jet. As seen in Table 1, with the slit jet, the peak overpressure is decreased on average by 12% and its standard deviation is vastly increased by 27% of the mean value of $\Delta p_{m,0}$ which is obtained without the slit jet. Similar characteristics were obtained by Lipkens and Blackstock [14], who used a rectangular slit with a typical width of 25.4 mm to generate the turbulent shear flow. The mean value of the peak overpressure in their experiment is

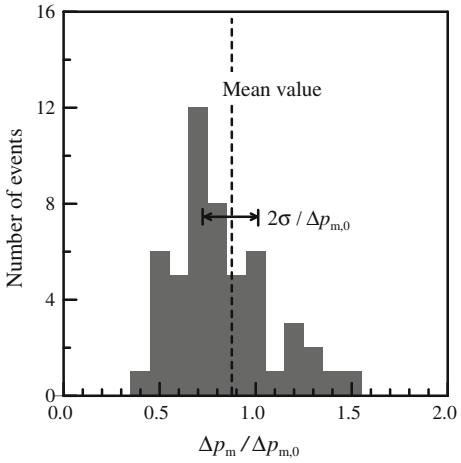

Fig. 7 Histogram of peak overpressure values over 50 operations with slit jet

Table 1 Statistical results for Δp_m

	Mean value (kPa)	σ (kPa)
Without slit jet	3.11	0.03
With slit jet	2.73	0.85

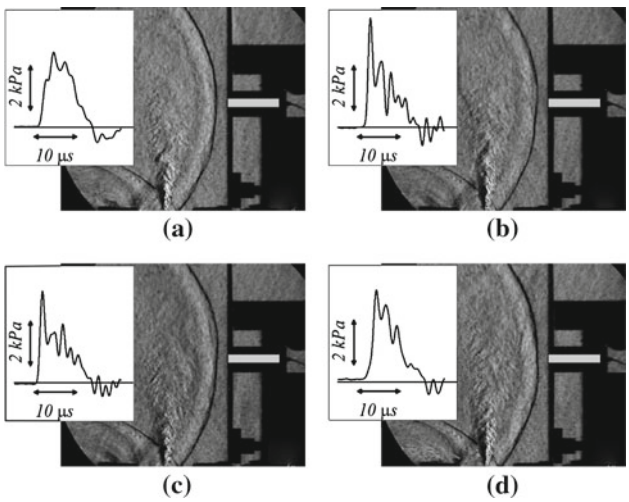

Fig. 8 Δp histories and corresponding shock wave configurations at $t = 336\,\mu s$, strong case

130.5 Pa. When a spherical shock wave propagated through the slit jet, the peak overpressure was decreased on average by 10%; its standard deviation approached 29% of $\Delta p_{m,0}$.

Several modulation types of the peak overpressure and corresponding numerically enhanced schlieren images at $t = 336\,\mu s$ are presented in Figs. 8 (strong case) and 9 (weak case). The relationships between overpressure history

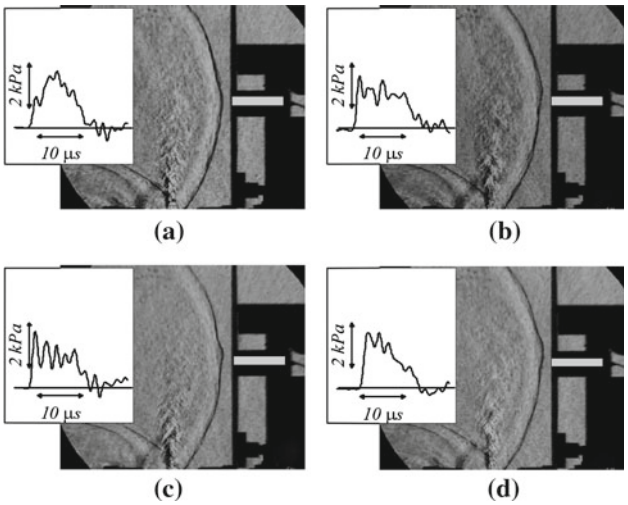

Fig. 9 Δp histories and corresponding shock wave configurations at $t = 336\,\mu$s, weak case

and shock wave deformation seen in Figs. 4 and 5 are clearly reproduced. In the strong cases of Fig. 8, where the peak overpressure exceeds the nominal value, in all cases the shock front has a flat shape in front of the pressure transducer. On the other hand, the shock front has a hump in the weak cases of Fig. 9. In both cases overpressure modulations after the peak value have various patterns; peaked type (Fig. 8b–d), rounded type (Figs. 8a, 9a, d), multi peaked type (Fig. 9b, c). In none of the experiments, a transition between the strong and weak cases was observed.

The shock wave distortions and overpressure modulations observed in this study seem to have the same characteristics that appear in shock-vortex interaction [7]. The variations of the thermodynamic properties across a shock front depends on the relative velocity between the shock and the medium. When a shock wave propagates in a region where the flow velocity is in the same direction, the relative shock velocity is decreased, and consequently the overpressure drops because the shock Mach number relative to the upstream gas becomes decreased. On the other hand, when a shock wave propagates in a region of opposite flow velocity, the relative velocity of shock is increased; the overpressure is increased because the shock Mach number is increased. In this case, a stationary observer of the expanding front observes a flattening of the front. However, in the cases of the present study the shock wave propagates through a complicated velocity field with spatio-temporal fluctuations. Many interactions occur at fine scales. The observed shock behavior is a result of integration of the interactions over the shear layer. The above-mentioned phenomenological explanation needs to be refined by better characterizing instant turbulent flow fields in the slit jet and by better diagnosing the interaction with the shock wave, which is beyond the scope of the present study.

4 Conclusion remarks

This study experimentally confirmed a clear relationship between the overpressure modulation and local shock front deformation in weak shock wave-turbulence interaction. When the peak overpressure was increased, the shock front became locally flat, and the local curvature was decreased. When the peak overpressure was decreased, the shock front developed a hump shape, and the local curvature oscillated strongly. Shock wave modulations through regions of non-uniform velocity should be better diagnosed with finer spatial and temporal resolution, so that microscopic shock-vortex interactions can be related with the macroscopic shock wave behavior patterns such as those observed in the present study. This challenging scope warrants further investigations.

Acknowledgments The authors would like to thank Prof. Takeharu Sakai, Department of Aerospace Engineering, Nagoya University, for helpful comments on the measurement of turbulent flow field. We also appreciate Professors Yasuhiko Sakai, Koji Nagata, and Dr. Takashi Kubo, Department of Mechanical Engineering, Nagoya University, for their cooperation in conducting hot-wire calibration. This work was supported by the Global Center of Excellence (GCOE) program for "Education and Research for Micro-Nano Mechatronics" in Nagoya University, and by the Japan Society for Aeronautical and Space Sciences.

References

1. Ben-Dor, G.: Shock Wave Reflection Phenomena, 2nd edn, chap. 3. Springer, Berlin (2007)
2. Colella, P., Henderson, L.F.: The von Neumann paradox for the diffraction of weak shock waves. J. Fluid Mech. **213**, 71–94 (1990)
3. Niedzwiecki, A., Ribner, H.S.: Subjective loudness of minimized sonic boom waveforms. J. Acoust. Soc. Am. **64**, 1617–1621 (1978)
4. Bass, H.E., Layton, B.A., Bolen, L.N., Raspet, R.: Propagation of medium strength shock waves through the atmosphere. J. Acoust. Soc. Am. **82**, 306–310 (1987)
5. Takayama, K., Sasoh, A., Onodera, O., Kanako, R., Matsui, Y.: Experimental investigation on tunnel sonic boom. Shock Waves **5**, 127–138 (1995)
6. Ribner, H.S.: Cylindrical sound wave generated by shock-vortex interaction. AIAA J. **23**(11), 1708–1715 (1985)
7. Ellzey, J.L., Henneke, M.R., Picone, J.M., Oran, E.S.: The interaction of a shock with a vortex:shock distortion and the production of acoustic waves. Phys. Fluids **7**(1), 172–184 (1995)
8. Chatterjee, A.: Shock wave deformation in shock-vortex interactions. Shock Waves **9**, 95–105 (1999)
9. Minota, T.: Interaction of a shock wave with a high-speed vortex ring. Fluid Dyn. Res. **12**, 335–342 (1993)
10. Minota, T., Kambe, T., Murakami, T.: Acoustic Emission from interaction of a vortex ring with a sphere. Fluid Dyn. Res. **3**, 357–362 (1988)
11. Ribner, H.S., Morris, P.J., Chu, W.H.: Laboratory simulation of development of superbooms by atmospheric turbulence. J. Acoust. Soc. Am. **53**, 926–928 (1973)
12. Pierce, A.D.: Spikes on sonic boom pressure waveforms. J. Acoust. Soc. Am. **44**, 1052–1061 (1968)

13. Pierce, A.D., Maglieri, D.J.: Effects of atmospheric irregularities on sonic-boom propagation. J. Acoust. Soc. Am. **51**(2), 702–721 (1972)
14. Lipkens, B., Blackstock, D.T.: Model experiments to study sonic boom propagation through turbulence, part 1: general results. J. Acoust. Soc. Am. **103**(1), 148–158 (1998)
15. Biringen, S., Howard, J.E., Reichert, R.S.: Simulation of sonic boom interaction with shear turbulence. Mech. Res. Commun. **32**, 604–609 (2005)
16. Sakai, Y., Watanabe, T., Kamohara, S., Kushida, T., Nakamura, I.: Simultaneous measurements of concentration and velocity in a CO_2 jet issuing into a grid turbulence by two-sensor hot-wire probe. Int. J. Heat Fluid Flow **22**, 227–236 (2001)
17. Liang, S.M., Hsu, J.L., Wang, J.S.: Numerical study of cylindrical blast-wave propagation and reflection. AIAA J. **39**(6), 1152–1158 (2001)